ChemComm
Chemical Communications

Accepted Manuscript

This article can be cited before page numbers have been issued, to do this please use: S. Wang, S. Zhang, X. Jia, X. Yan, Y. Tang, M. Kan, C. Liu and C. Xu, *Chem. Commun.*, 2026, DOI: 10.1039/D5CC06597F.

ROYAL SOCIETY OF CHEMISTRY

rsc.li/chemcomm

ChemComm

View Article Online
DOI: 10.1039/D5CC06597F

COMMUNICATION

A pH-responsive iron/manganese bimetallic organic frameworks nanosystem for synergistic therapy of colon cancer

Siyuan Wang [a], Shichen Zhang [b], Xue Jia [a], Xinran Yan [a], Yixin Tang [a] Mujie Kan [a], Chang Liu *[c] and Caina Xu *[a]

Received 00th January 20xx,
Accepted 00th January 20xx

DOI: 10.1039/x0xx00000x

The system, loaded with mitoxantrone (MTO) and encapsulated in sodium alginate (SA), achieved efficient drug delivery and tumor microenvironment-triggered release This release of MTO further exerted its chemotherapeutic effects and, in conjunction with ferroptosis, induced immunogenic cell death. This study provided a promising multifunctional nanoplatform for synergistic therapies of colon cancer.

Colon cancer is one of the most common malignant tumours worldwide, with the third in the number of new cases of all malignant tumours and second in the number of death.[1] Due to the high recurrence rate of the colorectal tumour, low specificity of treatment and toxic side effects, patients with advanced colon cancer often have a poor prognosis.[2] Although traditional methods such as surgery, radiotherapy, and chemotherapy have improved patient survival to a certain extent, traditional chemotherapy regimens still face challenges such as drug resistance, high systemic toxicity, and difficulty in accurately targeting tumour cells. Therefore, the development of new anticancer strategies that can simultaneously target the tumour microenvironment and activate the body's immune system has become a key research direction.

In response to the above challenges, ferroptosis, as a non-cystine-dependent programmed cell death method, has shown unique therapeutic potential. Ferroptosis, a programmed cell death pathway accompanied by iron-mediated lipid peroxidation (LPO), has attracted much attention because of its great potential in anticancer therapy. During ferroptosis, depletion of glutathione (GSH) decreases glutathione peroxidase 4 (GPX4) activity and leads to impaired cellular antioxidant capacity. Under the catalysis of the Fenton/Fenton-like reaction mediated by metal ions such as Fe/Mn, reactive oxygen species (ROS) accumulate in large quantities, which in turn triggers lipid peroxidation and ultimately induces ferroptosis.[3] More critically, cancer cells undergoing ferroptosis are usually accompanied by immunogenic cell death (ICD) and the anticancer drug mitoxantrone (MTO) can not only inhibit tumour growth, but also induce ICD.[4] The ICD induces the release of damage-associated molecular pattern (DAMP), which is a key component in the development of cancer cells. Mainly including calreticulin (CRT) exposure and high mobility group box 1 (HMGB1) release.[5] This ultimately produces a powerful anti-tumour immune response. In order to overcome the delivery bottlenecks of traditional chemotherapy drugs (such as instability in the body and lack of targeting), we use metal-organic frameworks (MOFs) materials to load chemotherapy drugs and achieve the synergistic therapeutic effect of ferroptosis and ICD.

Based on the synergistic therapeutic concept of ferroptosis, ICD and the excellent performance of MOFs, we designed and constructed a novel composite nano-delivery system, FMMS NPs, which loaded the anticancer drug MTO in the porous structure of Fe/Mn bimetallic MOFs and used sodium alginate (SA) for surface modification (Fig. 1). The FMMS NPs was decomposed in the acidic reducing conditions of the tumour microenvironment, releasing Fe and Mn ions. These ions could catalyse the generation of ROS *via* Fenton and Fenton-like reactions, and the down-regulation of GPX4, which triggered LPO and ultimately ferroptosis. At the same time, ferroptosis iron metastasis also effectively induced ICD in tumour cells, and in addition, the loaded MTO could be released at the tumour sites to directly kill tumour cells. MTO could effectively induce ICD in tumour cells. The multifunctional nano-delivery system of FMMS NPs based on Fe/Mn bimetallic MOFs developed in this study could release metal ions and MTO into the tumour microenvironment to synergistically induce ferroptosis and ICD, which provided a promising new synergistic therapeutic strategy for refractory malignant tumours such as colorectal cancer.

[a] College of Basic Medical Sciences, the Medical Basic Research Innovation Centre of Airway Disease in North China, Key Laboratory of Pathobiology, Ministry of Education, Jilin University, Changchun, 130021, China.
[b] Department of Oral and Maxillofacial Surgery, School and Hospital of Stomatology, Jilin University, Changchun, 130021, China.
[c] Department of Neurology and Neuroscience Centre, First Hospital of Jilin University, Changchun, 130021, China.

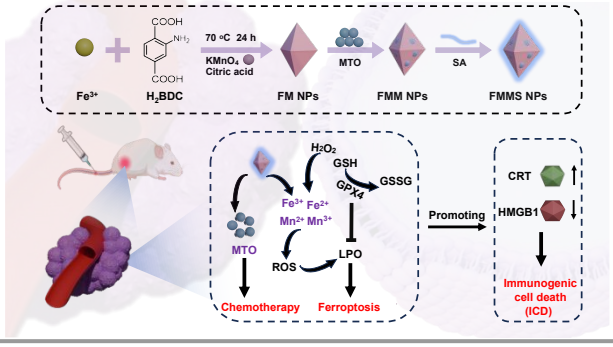

Fig. 1 Schematic representation of the synthesis of FMMS nanoparticles and schematic diagram of the mechanism of cancer treatment via chemotherapy, ferroptosis and ICD.

The synthesis method of metal organic frameworks (FM NPs) was carried out according to the literature.[6] The obtained product was washed three times with ethanol and distilled water respectively, and then the manganese element was introduced by $KMnO_4$ and citric acid reduction to obtain FM NPs. Subsequently, mitoxantrone (MTO) was loaded into FM NPs by simple stirring to obtain FMM NPs. By adjusting the feed ratio of FM NPs to MTO, FMM NPs with different MTO loading amounts could be prepared. The results showed that the drug loading was desired when the ratio of FM NPs and MTO was 4:1.5, and the MTO encapsulation efficiency was about 26 % measured by UV-VIS spectrophotometer (Table S1). Finally, the MOFs structure was stabilized by loading sodium alginate (SA) molecules on the surface to obtain the final products were FMMS NPs.

Scanning electron microscopy (SEM) characterization showed (Fig. 2A, S1) that FMMS NPs showed a uniform rhombus morphology with a size of 211.0±4.2 nm. We also used SEM to examine the morphology of FM NPs and found no significant changes before and after drug loading (Fig. S2). Zeta potential of FM NPs was (-16.1±3.7 mV), and after stirring the addition of MTO (-22.4±9.0 mV), the zeta potential of FMMS NPs was reduced to (-23.3±1.3 mV), which indicated that the MTO was successfully encapsulated in the MOFs. After modification with SA, the zeta potential of FMMS NPs changed to (-28.0±1.3 mV), which was attributed to the introduction of -OH groups in SA, confirming that SA had been successfully coated on the surface of FMM NPs (Fig. 2B). This negatively charged surface property contributes to the stability and biocompatibility of the nanoparticles in blood circulation.[7] The Brunauer-Emmett-Teller (BET) method showed that the specific surface area of FMMS NPs (204.02 m^2/g) was reduced compared to FM NPs (374.99 m^2/g), which also demonstrated that MTO was successfully loaded in the pores of FM NPs and effective modification of FMM NPs by SA (Fig. 2C). X-ray photoelectron spectroscopy (XPS) demonstrated that FMMS NPs were mainly composed Fe, Mn, N, O and other elements (Fig. S3A). The fine spectrum of the Mn element (Fig. S3B) showed that the binding energy peaks at 641.5 eV (Mn 2p3/2) and 652.9 eV (Mn 2p1/2) correspond to Mn^{3+} while the peaks at 642.9 eV (Mn 2p3/2) and 654.2 eV (Mn 2p1/2) correspond to Mn^{4+}.[8] Similarly, the presence of Fe^{3+} (Fig. S3C) was confirmed by the presence of Fe^{3+} through the presence at 721.4 eV (Fe 2p3/2) and 726.0 eV (Fe 2p1/2). The occurrence of Fe^{2+} was verified at 710.7 eV (Fe 2p3/2) and 724.3 eV (Fe 2p1/2).[9] In addition, the characteristic peaks at 399.7 eV and 401.3 eV correspond to -NH_2 of H_2BDC and C-N of MTO, respectively (Fig. S3D).[10] The O 1s spectrum (Fig. S3E) showed that the peaks at 532.7 eV and 529.8 eV correspond to the C=O and -OH groups in MTO, respectively; The peak at 531.3 eV was attributed to the -COOH in H_2BDC.[11] These XPS results further confirmed the successful loading of MTO.

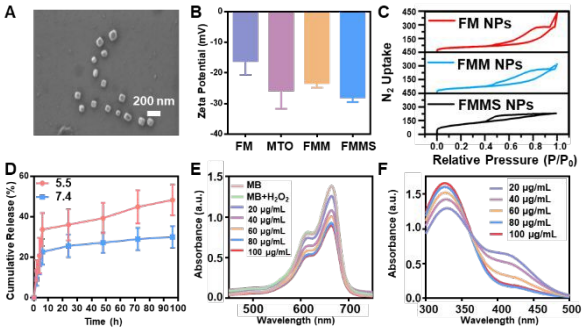

Fig. 2 (A) SEM image of FMMS NPs. (B) The zeta potential of FM NPs, MTO, FMM NPs, and FMMS NPs (n=3). (C) The Nitrogen absorption curves of FM NPs, FMM NPs, and FMMS NPs. (D) Cumulative release of MTO from FMMS NPs under different conditions (n=3). (E) Concentration-dependent spectra of MB mediated with FMMS NPs. (F) GSH consumption and GSSG generation.

As shown in Fig. 2D, the release amount of MTO from FMMS NPs increased significantly under lower pH conditions. This indicated that FMMS NPs exhibited pH-responsive drug release properties in the acidic microenvironment of tumours, which was beneficial to enhance the targeted delivery of anti-tumour drugs *in vivo* and reduce the burst effect under normal physiological conditions.

MB is used as an indicator for detecting ·OH generation. As shown in Fig. 2E, after incubation of different concentrations of FMMS NPs with MB for 30 min, the absorbance of MB showed a concentration-dependent decrease, confirming the ability of FMMS NPs to degrade MB, reflecting its ability to generate ROS. In addition, GSH, an intracellular antioxidant, protects cells from damage caused by ROS,[12] it was worth noting that FMMS NPs can effectively consume GSH. The DTNB method was used to detect the GSH content (characteristic absorption peak at 412 nm).[13] It showed that the absorbance of GSH decreased with the increase in the concentration of FMMS NPs (Fig. 2F).

As shown in Fig. 3A, RhB red fluorescence was observed in CT26 cells, and the intensity of red fluorescence with prolonged incubation, demonstrating that FMMS NPs were effectively internalized by CT26 cells in a time-dependent manner, which underlies their significant anti-tumor effects. Inspired by the excellent cellular uptake properties, MTT assays were performed on CT26 cells to determine the cytotoxicity of FMMS NPs under different conditions. As

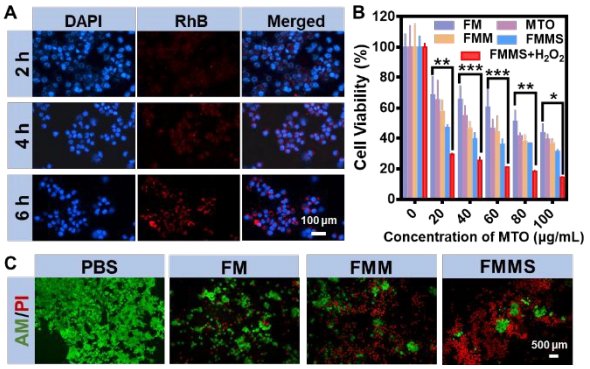

Fig. 3 (A) Fluorescence images of CT26 cells incubated with FMMS NPs at different time points. (B) Cell viability after incubation with nanoparticles or drugs at different concentrations for 24 h (n = 3). (C) Photographs of live/dead cell staining of CT26 cells under different conditions. Statistical significance was set as follows: $*p < 0.05$, $**p < 0.01$, $***p < 0.001$, $****p < 0.0001$.

showed in Fig. 3B, compared with FM NPs, FMM NPs loaded with MTO exhibited significant tumor cell cytotoxicity.

Notably, FMMS NPs exhibited superior cytotoxicity compared to FMM NPs, likely due to the enhanced dispersibility of SA loading, which in turn enhanced their biological efficacy. Furthermore, the MTT assay was used to examine the compatibility of FM NPs, MTO, FMM NPs, and FMMS NPs with NH3T3 cells and L929 cells. Results showed that at a concentration of 40 μg/mL, FMMS NPs did not cause significant damage to NH3T3 cells and L929 cells (Fig. S4, S5), demonstrating their excellent biosafety.

As shown by the MTT results, the FMMS NPs group exhibited the strongest anti-tumor effect (Fig. 3C). Wound healing assays are a simple and effective method to study cell migration *in vitro*, mimicking to some extent the process *in vivo*.[14] We investigated the effect of FMMS NPs on the migration of CT26 cells using a wound healing assay (Fig. S6A). Compared with PBS, FM NPs, and FMM NPs, the FMMS NPs-treated group exhibited a significantly lower healing rate, demonstrating their effective inhibition of CT26 cell migration. Furthermore, a colony formation assay revealed that the number of cell colonies formed in the FMMS NPs-treated group was significantly lower than in the other groups, indicating that FMMS NPs significantly inhibited CT26 cell proliferation (Fig. S6B). We have now performed comparative wound healing assays using L929 cells. The experiments demonstrate that the same nanoparticles exhibit no significant inhibitory effect on L929 cell migration (Fig. S7).

The results showed that after incubation with FMMS NPs for 4 h, the cells showed significantly enhanced red fluorescence (Fig. S8), indicating that FMMS NPs could effectively release Fe^{2+} and accumulate it in the cells.

The DCFH-DA method and flow cytometry were used to detect the intracellular ROS level. It was found that the green fluorescence intensity of CT26 cells in the FMMS NPs-treated group was significantly higher than that in the control group (Fig. S9A-C), confirming that FMMS NPs could induce a large amount of ROS generation by relying on metal ion components. Further immunofluorescence and Western blot analysis of GPX4 expression showed that the GPX4 protein level in the FMMS NPs-treated group was significantly downregulated (Fig. S10A-C), which was speculated to be related to its strong GSH depletion ability, thereby leading to GPX4 inactivation.

One of the important features of ferroptosis is lipid peroxidation.[15] One of the natural end products of lipid peroxidation is MDA, and to confirm lipid peroxidation, we measured the amount of MDA, which indicates the level of LPO in the cells.[16] Cells treated with FMMS NPs exhibited higher MDA levels compared to controls (Fig. S11), which indicated FMMS NPs could generate ROS and trigger the inactivation of GPX4, leading to lipid peroxidation and thus ferroptosis. Moreover, ferroptosis is often accompanied by mitochondrial dysfunction, especially a decrease in mitochondrial membrane potential (MMP).[17] JC-1 probe detection revealed increased green fluorescence and decreased red fluorescence in cells treated with FMMS NPs (Fig. S12), indicating decreased MMP activity and severe mitochondrial damage.

To validate the *in vitro* immune activation performed by FM NPs, two representative biomarkers of ICD effects, CRT and HMGB1, were first evaluated by immunofluorescence assay. The results showed that green fluorescence of CRT expression was evident on the surface of CT26 cells treated in the FM NPs group, whereas no green fluorescence was detected in the control group (Fig. S13A). Meanwhile, the green fluorescence of the nuclear protein HMGB1 was significantly attenuated by FM NPs (Fig. S13B), suggesting that iron death mediated a significant ICD effect due to the presence of Fe/Mn bimetallic. MTO can also contribute to ICD. Compared to the FM NPs group, the group loaded with MTO exhibited stronger CRT fluorescence and weaker HMGB1 green fluorescence, suggesting that MTO can also lead to ICD (Fig. S13A-B). Secondly, Western blot detection of CRT and HMGB1 expression in CT26 cells was consistent with the immunofluorescence results (Fig. S13C-E).

The animal study was approved and reviewed by the Research Ethics Committee of Jilin University. *In vivo* imaging results showed that Cy5-labeled FMMS NPs were effectively accumulated in the tumor sites of CT26 tumor-bearing mice following intravenous injection, reaching a peak concentration at 48 h, demonstrating excellent tumor targeting (Fig. S14). To systematically evaluate the efficacy, tumor-bearing mice were randomly divided into five groups and treated with PBS, FM NPs, MTO, FMM NPs, and FMMS NPs (Fig. 4A). The results showed that the FMMS NPs-treated group exhibited the strongest inhibitory effect on both tumor volume and mass (Fig. 4B-D). The FM NPs group exhibited some tumor growth inhibition, likely related to ferroptosis and its induced ICD effect. The superior efficacy of the FMMS NPs group was attributed to the synergistic mechanisms of chemotherapy, ferroptosis, and ICD. Furthermore, TUNEL and Ki-67 staining revealed that FMMS NPs significantly promoted tumor cell apoptosis and inhibited proliferation. Immunofluorescence analysis of tumor tissues revealed

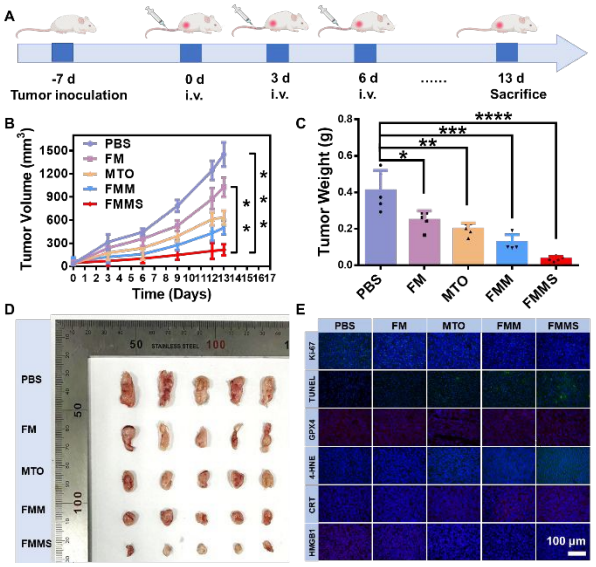

Fig. 4 (A) Schematic diagram of CT26 tumor-bearing mice received different treatment regimens. (B) The tumor growth curves of CT26 tumor-bearing mice after intravenous injection of various formulations (n=5). (C) The tumor weight of the mice in the different groups (n=5). (D) The photographs were obtained from mice at the end of treatment (E) The immunofluorescence analysis of Ki-67, TUNEL, GPX4, 4-HNE, HMGB1, and CRT levels in tumors harvested from different groups. Statistical significance was set as follows: $*p < 0.05$, $**p < 0.01$, $***p < 0.001$, $****p < 0.0001$.

downregulation of GPX4 expression, increased 4-HNE levels, upregulation of CRT expression, and HMGB1 release in the FMMS NPs-treated group (Fig. 4E).

In terms of safety, we used several different approaches to investigate the biosafety of FMMS NPs. The results showed that the body weight of tumor-bearing mice in each group remained stable during treatment (Fig. S15), suggesting that FMMS NPs had no significant effect on mouse growth. *In vitro* hemolysis experiments showed that the hemolysis rate of FMMS NPs remained low within the concentration range of 20 to 100 μg/mL (Fig. S16), demonstrating their excellent hemocompatibility and safety for intravenous injection. Further blood biochemical analysis revealed no significant fluctuations in key parameters (Fig. S17-S22). Furthermore, H&E stained tissue sections of major organs showed no obvious pathological damage (Fig. S23).

In summary, this study successfully constructed a novel nano-delivery system (FMMS NPs) based on a Fe/Mn bimetallic MOFs and encapsulated with SA. This system achieved efficient loading of the chemotherapeutic drug MTO and controlled release responsive to the tumor microenvironment. Mechanistic studies revealed that, upon internalization by tumor cells, FMMS NPs catalyzed H_2O_2 to generate ROS and downregulate GPX4 expression, synergistically inducing ferroptosis. Simultaneously, the loaded MTO exerted a chemotherapeutic effect, and in conjunction with ferroptosis, triggered ICD. *In vitro* and *in vivo* experiments confirmed that this synergistic combination of chemotherapy, ferroptosis, and ICD endowed FMMS NPs with potent antitumor activity, and systematic safety assessments demonstrated their excellent biocompatibility.

The authors are thankful to the Jilin Province Science and Technology Development Program (20230101045JC), and the Fundamental Research Funds for the Central Universities (2025-JCXK-28).

CRediT authorship contribution statement

Siyuan Wang: Writing - original draft, Data curation. Shichen Zhang: Data curation. Xue Jia: Data curation. Xinran Yan: Data curation. Yixin Tang: Data curation. Mujie Kan: Writing - review & editing. Chang Liu: Writing - review & editing. Caina Xu: Writing - review & editing.

Conflicts of interest

There are no conflicts to declare.

Data availability

The data supporting this article have been included as part of the Supplementary Information.

Notes and references

1 E. Morgan, M. Arnold, A. Gini, V. Lorenzoni, C.J. Cabasag, M. Laversanne, J. Vignat, J. Ferlay, N. Murphy and F. Bray, *Gut*, 2023, **72**, 338-344
2 M. Zahra, U. B. Zahra, H. Abrahamse and B. P. George, *RSC Adv.*, 2025, **15**, 37833-37855.
3 Y.W. Wei, Z.H. Wang, J. Yang, R. Xu, H.Z. Deng, S.Y. Ma, T.X. Fang, J. Zhang and Q. Shen, *J Colloid Interface Sci.*, 2022, **606**, 1950-1965.
4 J.H. Li, W.X. Lv, Z.W. Han, Y.K. Li, J.Q. Deng, Y.J. Huang, S. Wan, J.S. Sun and B. Dai, *Adv. Sci.*, 2025, **12**, 2501542.
5 X. Chen, R. Kang, G. Kroemer and D.L. Tang, *Nat. Rev. Clin. Oncol.*, 2021, **18**, 280-296.
6 C. Wang, X.D. Jia, W.Y. Zhen, M.C. Zhang and X. Jiang, *ACS Biomater. Sci. Eng.*, 2019, **5**, 4435-4441.
7 Z.Z. Feng, G. Chen, M. Zhong, L. Lin, Z.Y. Mai, Y. Tang, G.M. Chen, W. Ma, G. Li, Y.Y. Yang, Z.Q. Yu and M. Yu, *Biomaterials*, 2023, **302**, 122333.
8 L.M. Yu, Z. Mo, X.L. Zhu, J.J. Deng, F. Xu, Y.H. Song, Y.B. She, H.M. Li and H. Xu, *Green Energy Environ.*, 2021, **6**, 538-545.
9 W.F. Li, T. Zhang, L. Lv, Y.X. Chen, W.X. Tang and S.W. Tang, *Colloid Surface A*, 2021, **624**, 126791.
10 L. Guo, Y.X. Tang, L. Wang, R. Zhou, S.Y. Wang, H.Q. Xu, X. Yang, J.Z. Zhang, J. Chen, C.N. Xu, Y.H. Li and H.Y. Tian, *Adv. Funct. Mater.*, 2024, **34**, 2403188.
11 Z.W. You, Z. Wang, K.X. Tian and X.Y. Yao, *J. Environ. Chem. Eng.*, 2023, **11**, 110159.
12 T. Liu, L. Sun, Y.B. Zhang, Y.L. Wang and J. Zheng, *J. Biochem. Mol. Toxicol.*, 2022, **36**, e22942.
13 K.N. Zhang, H. Sun, L. Wei, R. Hu, H. Liu, Y.C. Lai and X. Li, *Spectrochim. Acta A*, 2025, **328**, 125439.
14 Y.M. Ma, X.H. Li, W.K. Hu, M.Y. Ruan, M. Yang, L.Q. Chang, H.R. Gu and C.Z. Hu, *Microsyst. Nanoeng.*, 2025, **11**, 134.
15 C.H. Liu, Z.H. Liu, Z. Dong, S.J. Liu, H.D. Kan and S.P. Zhang, *J. Genet. Genomics*, 2025, **53**, 1071-1081.
16 X. Zhang, L.C. Hou, Z. Guo, G.C. Wang, J.T. Xu, Z.H. Zheng, K. Sun and F.J. Guo, *Cell Death Discov.*, 2023, **9**, 320.
17 W. Chen, B. Wang, S.S. Liang, L.N. Zheng, H. Fang, S. Xu, T.F. Zhang, M. Wang, X. He and W.Y. Feng, *J Colloid Interface Sci.*, 2025, **680**, 261-273.

View Article Online
DOI: 10.1039/D5CC06597F

Data Availability Statement

The data supporting this article have been included as part of the Supplementary Information.